Supporting Information for "Vibrational properties of $CuInP_2S_6$ across the ferroelectric transition"

Sabine N. Neal,[1] Sobhit Singh,[2] Xiaochen Fang,[3] Choongjae Won,[4] Fei-ting Huang,[5]

Sang-Wook Cheong,[2, 3, 4] Karin M. Rabe,[2] David Vanderbilt,[2] and Janice L. Musfeldt[1, 6, ∗]

[1]*Department of Chemistry, University of Tennessee, Knoxville, Tennessee 37996, USA*

[2]*Department of Physics and Astronomy,*

Rutgers University, Piscataway, New Jersey 08854, USA

[3]*Rutgers Center for Emergent Materials,*

Rutgers University, Piscataway, new Jersey 08854, USA

[4]*Laboratory for Pohang Emergent Materials and Max*

Plank POSTECH Center for Complex Phase Materials,

Pohang University of Science and Technology, Pohang 790-784, Korea

[5]*Rutgers Center for Emergent Materials,*

Rutgers University, Piscataway, New Jersey 08854, USA

[6]*Department of Physics and Astronomy,*

University of Tennessee, Knoxville, Tennessee 37996, USA

(Dated: January 26, 2022)

∗ musfeldt@utk.edu

Vibrational mode assignments + symmetries from lattice dynamics calculations

Table S1 summarizes the modes expected in each phase of $CuInP_2S_6$. Tables S2 and S3 summarize our experimental and calculated infrared and Raman-active mode assignments for Type I single crystals of $CuInP_2S_6$. A short description of each mode displacement pattern is included as well. Figure S1 displays a comparison between experimental and theoretical mode frequencies for the $C2/c$ and Cc space groups. Good agreement is observed between theoretical predictions and experimental observations.

TABLE S1. Summary of mode symmetries expected in each phase of $CuInP_2S_6$.

Type of spectroscopy	High temperature paraelectric phase ($C2/c$)	Low temperature ferroelectric phase (Cc)
Infrared absorption	A_u, B_u	A', A''
Raman scattering	A_g, B_g	A', A''

FIG. S1. Comparison of the experimental data recorded at 325 ($\approx$ 300) K for $C2/c$ (Cc) phase of $CuInP_2S_6$ with the DFT-D3 calculated (a) infrared and (b) Raman-active phonon frequencies at $0\,$K. We note that LO - TO corrections were not considered in our DFT-D3 calculations, which are responsible for modest deviation of the theoretical data for infrared-active modes at higher frequencies from the diagonal line, *i.e.*, from the experimental data.
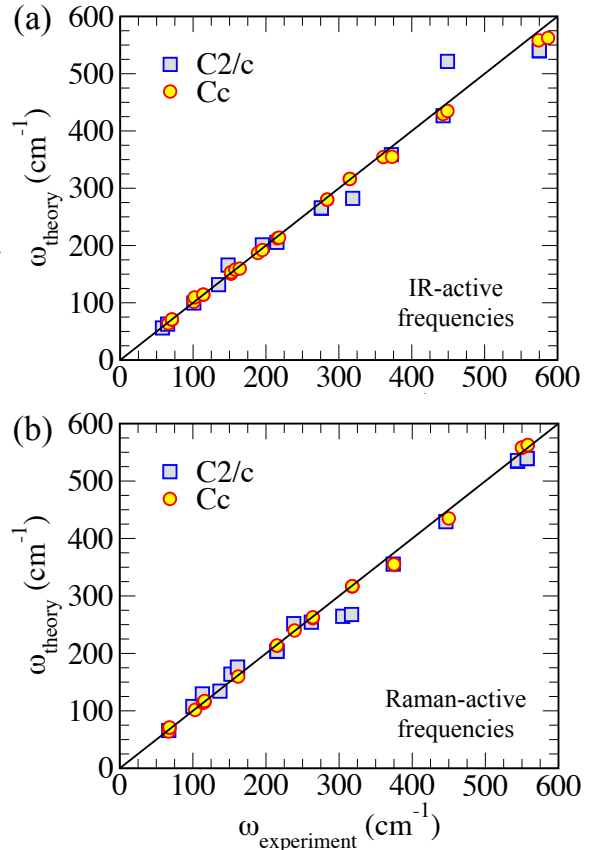
TABLE S2. Frequency of the infrared-active modes along with their vibrational assignments for single crystalline $CuInP_2S_6$. Corresponding DFT-D3 calculated mode frequencies are given in parentheses. All values are in units of cm^{-1}.

| $C2/c$		Cc		
Exp. (Theory)	Symmetry	Exp. (Theory)	Symmetry	Displacement patterns
58 (56.1)	A_u	-	-	in-plane Cu + out-of-plane S vibration
65 (62.8)	B_u	-	-	in-plane twist of P-P dimers + out-of-plane S vibration
-	-	66 (64.2)	A'	out-of-plane polar displacement of Cu
-	-	71 (70.5, 71.0)	A', A''	in-plane displacement of Cu + In + P + out-of-plane S
101 (99.6)	B_u	101, 102 (101.7, 109.4)	A', A''	rigid out-of-plane displacement of P-P dimers (in-phase in adjacent layers for A', and opposite phase for A'')
-	-	114 (114.1, 114.3)	A', A''	in-plane Cu + In, and out-of-plane S vibration
135 (131.7)	B_u	-	-	in-plane S vibration
148 (165.9)	B_u	-	-	rigid out-of-plane displacement of P-P dimers (in-phase in adjacent layers) + in-plane S vibration
-	-	151 (150.7, 153.4)	A', A''	in-plane Cu + In + P-P dimers, and out-of-plane S vibration
-	-	158, 164 (158.0, 159.7)	A'', A'	out-of-plane displacement of P-P dimers + in-plane S vibration
-	-	189 (187.0)	A''	in-plane displacement of Cu + P-P dimers + out-of-plane S vibration
195, 215 (201.1, 205.5)	A_u, B_u	195, 216, 218 (192.1, 212.7, 213.7)	A', A', A''	in-plane Cu + P + out-of-plane S vibration
276 (264.9, 265.7)	B_u, A_u	-	-	in-plane Cu + S vibration
-	-	284 (280.0, 280.3)	A', A''	in-plane Cu + P + S vibrations
319 (282.3)	B_u	-	-	out-of-plane P-P translation + out-of-plane S vibration
-	-	315 (316.1, 316.3)	A', A''	in-plane Cu + P + S vibrations
-	-	361 (354.4)	A'	in-plane Cu + S and out-of-plane P-P stretching (in-phase in adjacent layers)
372 (358.7)	A_u	373 (355.0)	A''	in-plane Cu + S and out-of-plane P-P stretching (opposite phase in adjacent layers)
443 (426.7)	B_u	443 (429.6)	A'	out-of-plane P-P translation + in-plane S vibration
449 (521.5)	A_u	449 (434.9)	A''	out-of-plane P-P + in-plane S vibration
574 (539.7, 540.6)	B_u, A_u	574, 587, 611 (558.2, 562.5, 562.7)	A'', A', A''	in-plane P-P + in-plane S vibration

TABLE S3. Frequency of the Raman-active modes along with their vibrational assignments for single crystalline $CuInP_2S_6$. Corresponding DFT-D3 calculated mode frequencies are given in parentheses. All values are in units of cm^{-1}.

C2/c		Cc		
Exp. (Theory)	Symmetry	Exp. (Theory)	Symmetry	Displacement patterns
67 (65.8)	B_g	-	-	in-plane P + out-of-plane S vibration
-	-	68, 67 (64.2, 70.5, 71.0)	A', A'', A''	out-of-plane Cu (polar for A' and antipolar for A'' displacements in the adjacent layers) + out-of-plane S vibration
100 (107.5)	B_g	-	-	rigid out-of-plane displacement of P-P dimers (opposite phase in adjacent layers) + In displacements opposite to that of P-P dimers
-	-	103 (101.7)	A'	rigid out-of-plane displacement of P-P dimers (in-phase phase in adjacent layers) + In displacements opposite to that of P-P dimers
113 (129.5)	A_g	114, 116 (114.1, 114.3, 115.5, 117.2)	A', A'', A', A''	in-plane displacement of Cu + In + S, out-of-plane S vibration
137 (134.3)	B_g	-	-	in-plane displacement of Cu + In + S
152 (163.8)	B_g	-	-	rigid out-of-plane displacement of P-P dimers (in-phase in adjacent layers for A', and opposite phase for A'')
161 (175.4, 176.2)	A_g, A_g	-	-	in-plane Cu + P and out-of-plane S vibration
-	-	162 (159.7)	A'	out-of-plane P-P + in-plane S vibration
215 (203.4, 203.8)	B_g, A_g	215 (213.4, 213.7)	A', A''	in-plane Cu + P, and out-of-plane S vibration
238, 262 (251.7, 254.3)	B_g, A_g	239 (239.9)	A'	in-plane Cu + P, and out-of-plane S vibration
-	-	264 (261.3, 262.9)	A', A''	in-plane S vibration
305 (264.6)	A_g	-	-	in-plane S vibration
317 (267.7)	B_g	318 (316.6, 316.8, 317.0)	A'', A', A''	in-plane P + S vibration
374 (355.4)	A_g	375 (354.4, 355.0)	A', A''	out-of-plane P + in-plane S vibration
446 (429.3)	B_g	450 (434.9)	A''	out-of-plane P + out-of-plane S vibration
544 (534.2, 535.6)	A_g, B_g	550 (558.1, 558.2)	A'', A'	in-plane P-P stretching + in-plane S vibration
557 (539.0, 539.3)	A_g, B_g	558 (562.5, 562.7)	A', A''	in-plane P-P + in-plane S vibration

Variable temperature infrared spectroscopy of single phase CuInP$_2$S$_6$

Figure S2 shows the complete infrared spectra across the range of 50 - 650 cm^{-1}. The low temperature spectra is in blue (10 K) and the high temperature is in red (325 K). An in-depth discussion on both ferroelectric and paraelectric phases is found in the main text.

FIG. S2. Variable temperature infrared spectra from 50 - 650 cm^{-1} of a pure phase Type I crystal. The blue represents the low temperature spectra, whereas the red represents high temperature phase spectra.
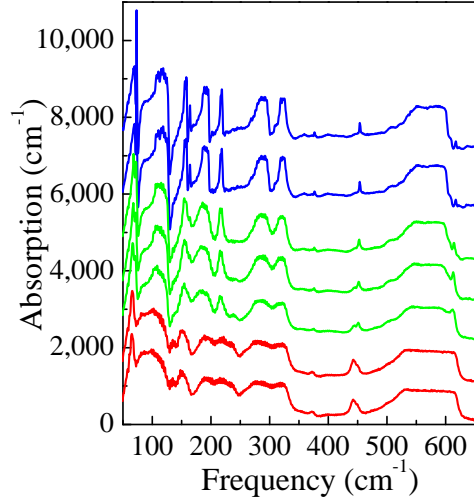
Hysteresis across T_C and T_g along with two-step behavior at T_g

Figure S3 displays variable temperature Raman measurements of CuInP$_2$S$_6$ with both increasing temperature (panels a and c) and decreasing temperature (panels b and d). The top panels highlight features from 150 - 350 cm^{-1}, whereas the bottom panels show the modes present over the 400 - 600 cm^{-1} range. Taking a closer look, we see that both T_C and T_g have clear hysteresis effects. The behavior across the relaxation/glassy transition is the most interesting. When measurements are taken with increasing temperature, T_g rises, and the two-step transition region narrows. The opposite is also true. When measuring with decreasing temperature, T_g drops slightly, and the two-step transition range broadens. There is also an increase in the background scattering across the transitions. A possible origin may be critical scattering (opalescence) from the micro-domains.

Tendency toward chemical phase separation in CuInP$_2$S$_6$-like materials

CuInP$_2$S$_6$ is just one stable phase amongst many available within the rich temperature-composition phase diagram of CuInP$_2$S$_6$-like materials. The majority of other chemically-related compounds have only slightly different compositions and follow the general formula Cu$_{1-x}$In$_{1+x/3}$P$_2$S$_6$ [S1]. This exceptional complexity makes growth of single crystals and quantum dots with the correct nominal composition quite challenging [S1, S2]. At the same
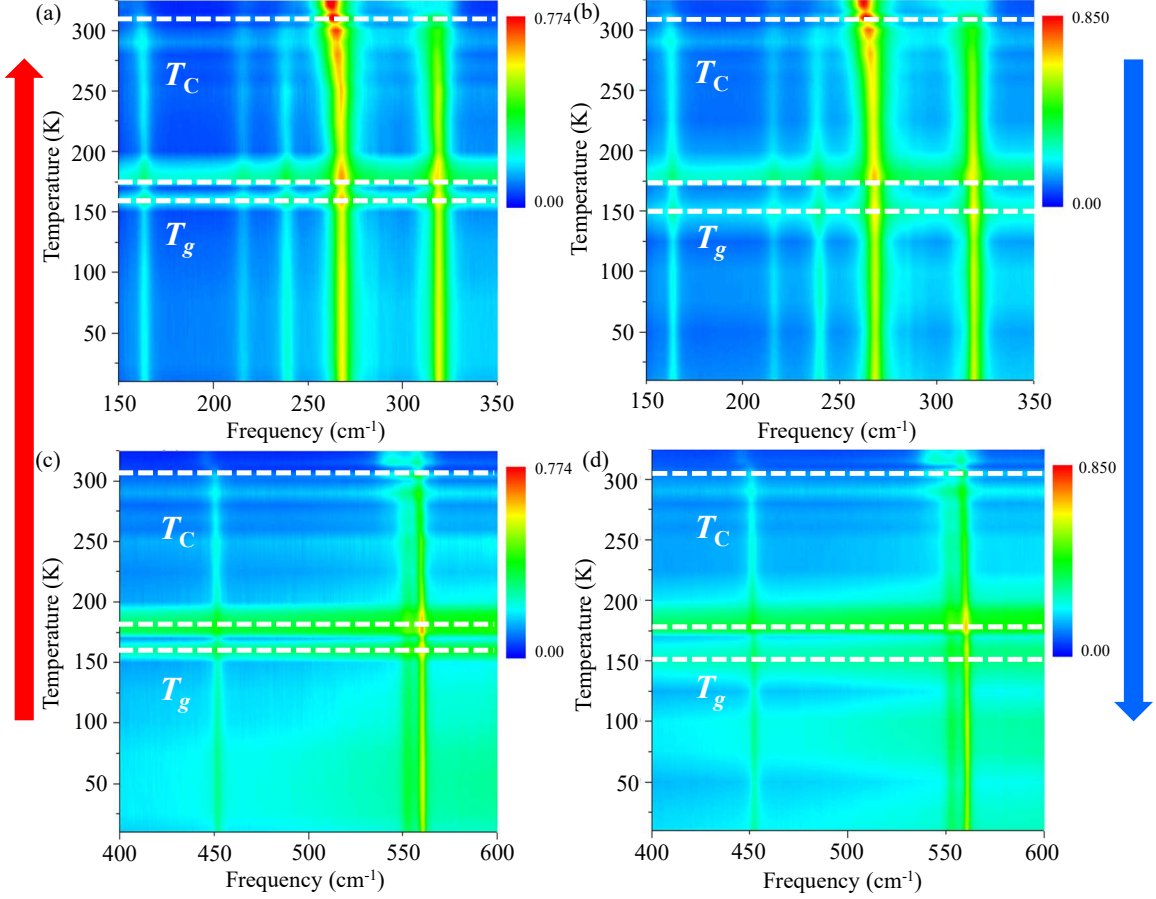
FIG. S3. Hysteresis effects in the Raman scattering response of phase pure (Type I) $CuInP_2S_6$. Panels (a, c) Raman measurements with increasing temperature; (b, d) with decreasing temperature. The top panels show features in the 150 - 350 cm^{-1} range, whereas the bottom panels highlight features in the 400 - 600 cm^{-1} range. The ferroelectric and glassy transitions are indicated by the dashed lines.

time, it is important to avoid phase segregation. Despite a number of prior reports, there is no consensus on the visual appearance of a high quality single crystal or the character of a Raman scattering spectrum at room temperature. This is because color changes with thickness, Cu concentration, and defect concentration, and a traditional Raman response averages over the presence of any chemical phase separation. Two principle varieties of Raman spectra have been reported for nominally stoichiometric crystals. One kind has well separated vibrational features whereas the other type has a more complicated pattern with clustered peaks [S3–S10]. As part of this work, we explored the origin of these differences in order to reveal the intrinsic properties of $CuInP_2S_6$. As described below, we uncover both

phase pure $CuInP_2S_6$ as well as crystals with a segregated impurity phase. The impurity phase material is $In_{4/3}P_2S_6$ [S1].

Chemical vapor transport growth of $CuInP_2S_6$ single crystals results in thin, orange, transparent flakes. We find, however, that two types of flakes with distinct thicknesses, colors, and sizes coexist - even in the same batch. Figure S4 shows a side by side comparison. The Type I flake has a lateral dimension of 0.5-1.0 mm and a thickness of 70-150 µm [Fig. S4 (a) left and (b)]. The color is homogeneous and darker than the other kind of crystal. Type II flakes, on the other hand, have a large lateral dimension (3-10 mm), reduced thickness (10-30 µm), and lighter color [Fig. S4 (a) right and (c)]. Figure S5(a,b) displays transmission optical microscope images of both specimens with $50\times$ magnification. The Type-I $CuInP_2S_6$ crystal has a homogeneous orange color without additional patterns whereas the Type-II crystal has wavy stripes with dark/bright contrast. The Type-I crystal is pure $CuInP_2S_6$ whereas the Type-II crystal type is mixed-phase.

FIG. S4. (a) Size comparison of the different types of crystal flakes. (b,c) $5\times$ Optical microscope images taken in bright field mode of (b) the type of flake with small lateral dimension and greater thickness (corresponding to the Type I pure phase system) and (c) the type of flake with large lateral dimension and lesser thickness (corresponding to the Type II mixed phase system).
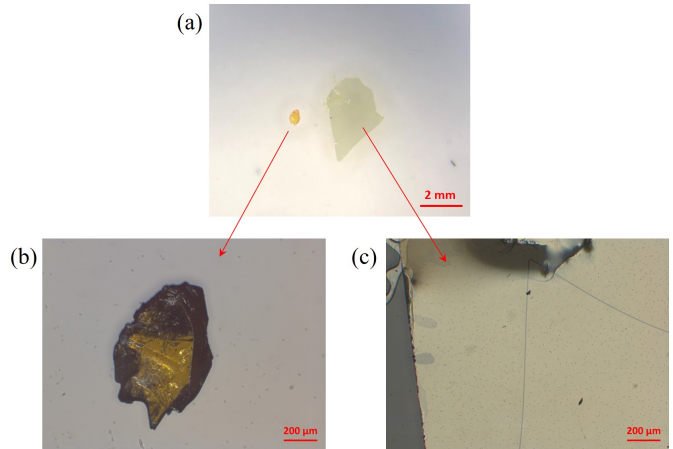
To understand the difference between the two types of $CuInP_2S_6$ and what causes the wavy stripes observed in the Type II sample, we took vertical piezo-force microscopy images on freshly exfoliated surfaces at room temperature. When the temperature is below T_C, $CuInP_2S_6$ exhibits a spontaneous polarization perpendicular to the layered planes which originates from the off-center ordering of the Cu sublattice and the slight displacement of In cations from the sulfur octahedral center [Fig. 1, main text]. This atomic arrangement gives rise to two possible ferroelectric variants with opposite polarization directions perpendicular to the layered planes.
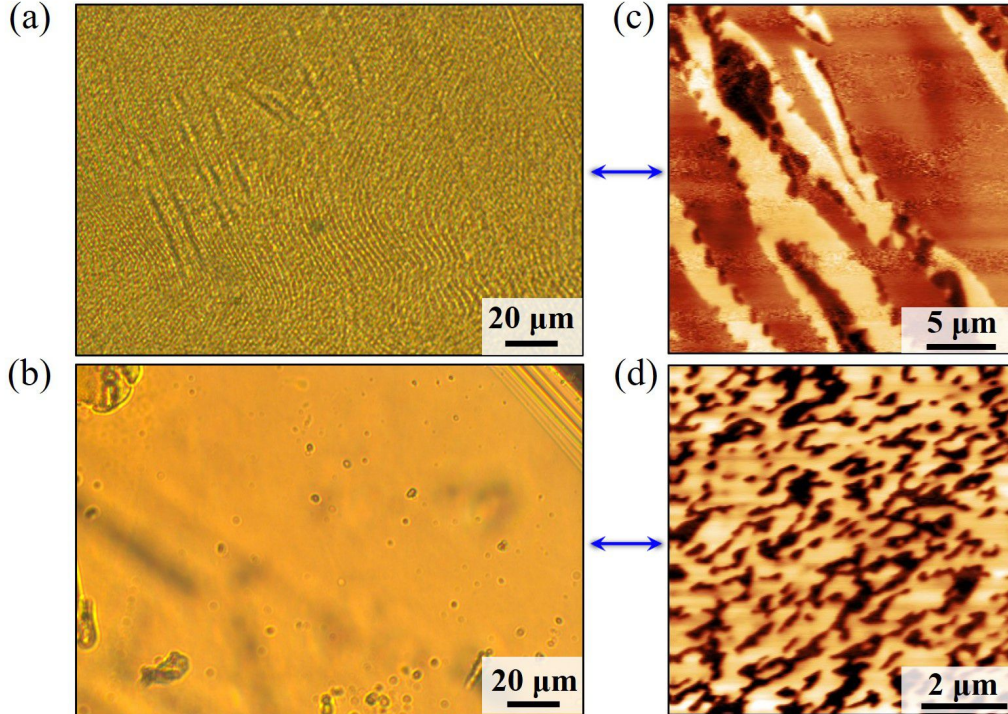
FIG. S5. (a, b) Comparison of optical microscope images taken in transmission for mixed-phase (Type II) and pure (Type I) $CuInP_2S_6$. (c, d) Vertical piezo-force microscopy images for mixed phase and pure $CuInP_2S_6$.

Figure S5(c,d) displays the vertical piezo-force microscopy images for the two specimens. For the Type II sample, we find two kinds of alternating wavy stripes and three kinds of coexisting domains. One type of stripe contains two domains showing dark and bright colors, whereas the adjacent stripes display a single color. The size of these stripes is comparable to those observed in the optical microscope image [Fig. S5(a)]. For the Type I sample, we find irregular island domains with two different colors. The two kinds of domains in the Type I sample should correspond to the two possible ferroelectric variants. As for the three kinds of domains in the Type II sample, since there exists only two possible ferroelectric variants [Fig. 1, main text], we can conclude that the Type II crystal contains a significant impurity phase in addition to the two separate phases that form into alternating wavy stripes. This impurity phase is directly confirmed to be Cu-deficient $In_{4/3}P_2S_6$ via transmission electron microscopy [S11]. Several other chemical phase separation patterns are shown in Fig. S6 for the Type II crystals.

Figure S7 shows the phase-separated image and selected area electron diffraction (SAED)
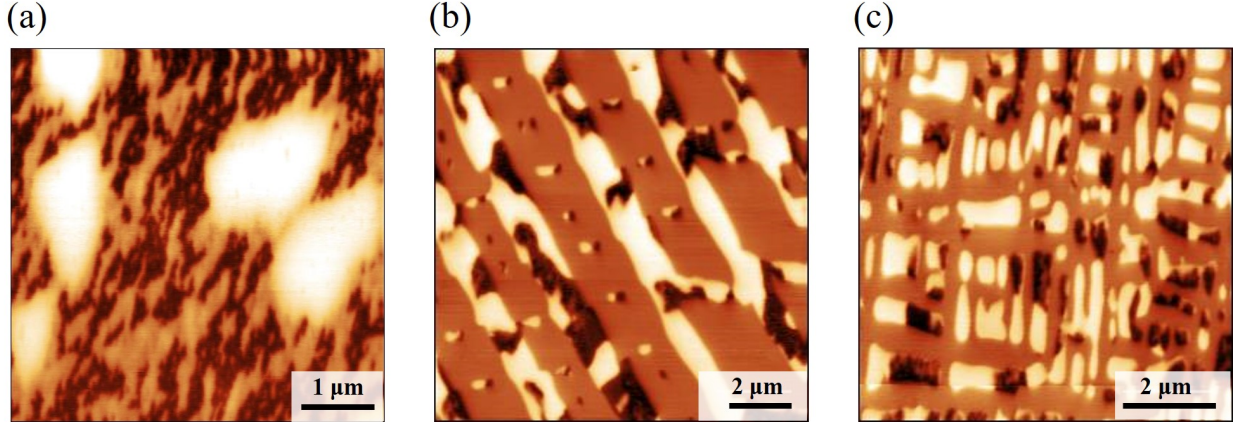
FIG. S6. Vertical piezo-force microscopy images of Type II crystals: (a) phase-separated $CuInP_2S_6$ showing impurity phase with circular shape, (b) phase-separated $CuInP_2S_6$ showing straight stripe patterns, (c) phase-separated $CuInP_2S_6$ showing rectangular block patterns.

patterns of Type II $CuInP_2S_6$ along [100] and [001], respectively. $In_{4/3}P_2S_6$ and $CuInP_2S_6$ coexist within the crystal by aligning along the b-axes to maintain the layered structural framework. Intriguingly, we find that phase-separated patterns of the Type II crystals vary a great deal and include alternating wavy stripes with circular inclusions, straight stripes, rectangular blocks, among others. Vertical piezo-force microscopy images showing these
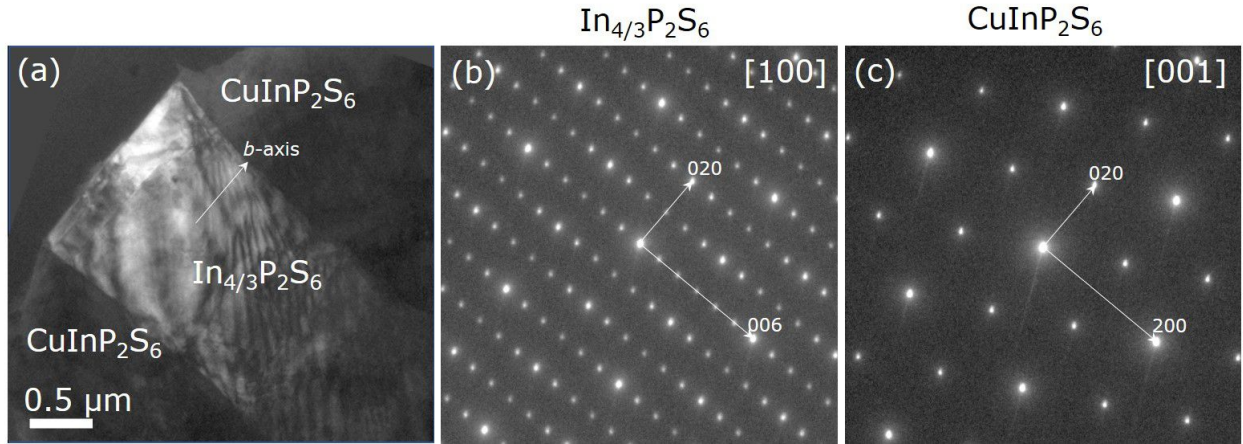

FIG. S7. (a) In-plane TEM images of a Type II $CuInP_2S_6$ crystal, revealing local phase separation. The bright and dark areas with sharp phase boundaries represent $In_{4/3}P_2S_6$ and $CuInP_2S_6$, respectively. Selected area electron diffraction patterns taken on regions of (b) $In_{4/3}P_2S_6$ and (c) $CuInP_2S_6$ shown in (a).

patterns can be seen in Fig. S6. Clearly phase separation can be quite robust. The domain size depends upon the cooling rate [S1].

Figure S8(a) summarizes the Raman response of $CuInP_2S_6$, a mixed phase crystal, and $In_{4/3}P_2S_6$. Clearly, the Raman scattering spectrum of the mixed phase sample is a superposition of the other two. Unfortunately, the spectrum of the mixed phase material appears very commonly in the literature [S4, S5, S8] - usually incorrectly identified as the pure phase $CuInP_2S_6$. As demonstrated above, a detailed analysis of composition, electron diffraction, and piezoforce microscopy was needed to unravel the situation, and now that we have linked these properties with the character of the Raman spectrum, phase identification will be much easier. Assuming that the spectrum of the mixed phase sample is a straightforward superposition of $CuInP_2S_6$ and $In_{4/3}P_2S_6$, we can estimate an impurity phase concentration by a simple ratio analysis [S14]. We find that the crystal with chemical phase separation may contain as much as 80% $In_{4/3}P_2S_6$. This analysis obviously assumes that the response of the mixed phase system is a linear combination of the characteristics of the two end
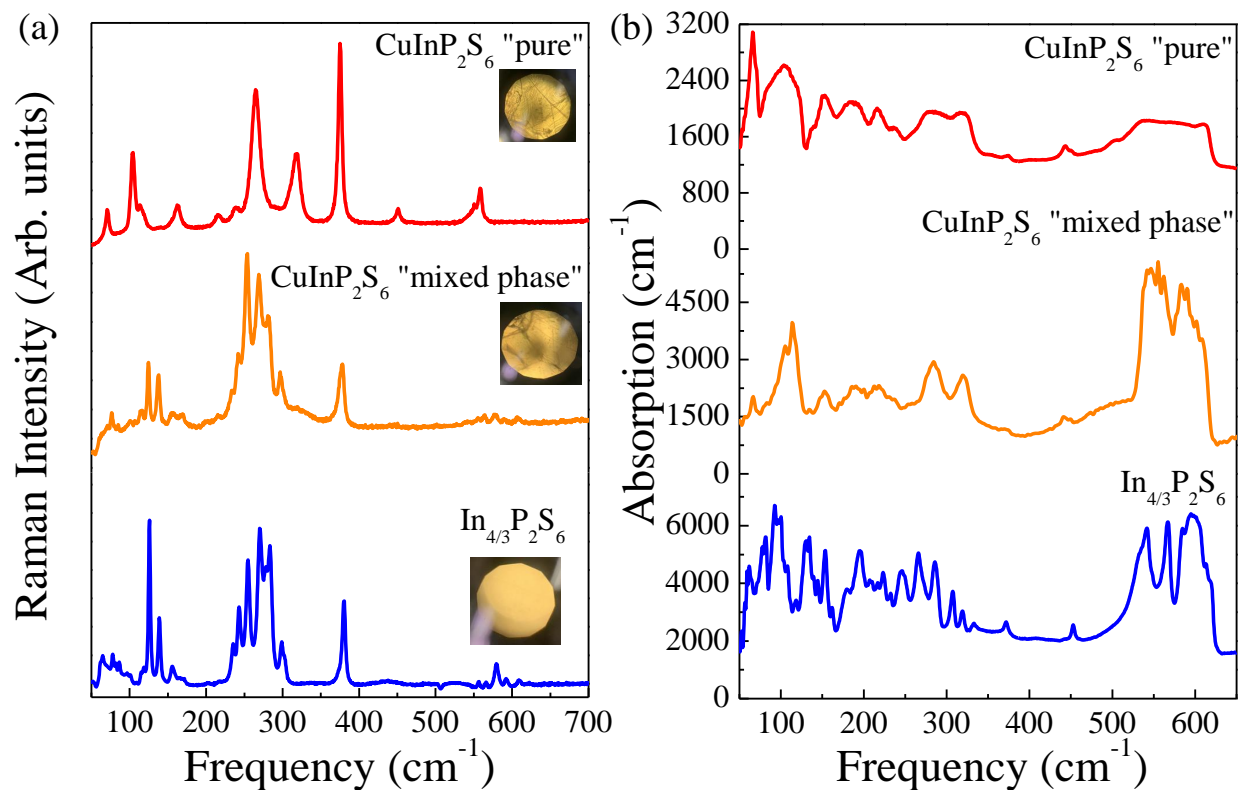

FIG. S8. Comparison of the (a) Raman scattering and (b) infrared absorption of the pure and mixed phase $CuInP_2S_6$ as well as the impurity phase $In_{4/3}P_2S_6$. All spectra are taken at 300 K.

members. Characteristic signatures of $In_{4/3}P_2S_6$ inclusions include: (i) a strong doublet centered between 125 and 145 cm^{-1} as well as (ii) a multi-peak cluster between 230 and 300 cm^{-1}. The spectrum of pure phase $CuInP_2S_6$ is simpler with well-separated peaks. The mode positions are also in good agreement with our dynamics calculations, which can be found in Tables S1 and S2. All of the work presented in this paper was performed on high quality, pure phase Type I $CuInP_2S_6$ single crystals.

Figure S8(b) shows the infrared absorption of phase pure (Type I) $CuInP_2S_6$, a mixed phase (Type II) sample, and $In_{4/3}P_2S_6$. Overall, the spectra are similar to what is found in the MPS_3 (M = Mn, Fe, Ni) series [S15] except for the additional modes activated due to the chemical and structural complexity on the metal site. Our mode assignments are summarized in Tables S1 and S2.

―――――――

[S1] M. A. Susner, M. Chyasnavichyus, M. A. McGuire, P. Ganesh, and P. Maksymovych. Adv. Mater. **29**, 1–39 (2017).

[S2] Y. Chen, S. Li, L. Huang, and D. Pan. Inorg. Chem. **52**, 7819–7821 (2013).

[S3] L. Niu, F. Liu, Q. Zeng, X. Zhu, Y. Wang, P. Yu, J. Shi, J. Lin, J. Zhou, Q. Fu, W. Zhou, T. Yu, X. Liu, and Z. Liu. Nano Energy **58**, 596–603 (2019).

[S4] M. A. Susner, M. Chyasnavichyus, A. A. Puretzky, Q. He, B. S. Conner, Y. Ren, D. A. Cullen, P. Ganesh, D. Shin, H. Demir, J. W. McMurray, A. Y. Borisevich, P. Maksymovych, and M. A. McGuire. ACS Nano **11**, 7060–7073 (2017).

[S5] A. V. Ievlev, M. A. Susner, M. A. McGuire, P. Maksymovych, and S. V. Kalinin. ACS Nano **9**, 12442–12450 (2015).

[S6] X. Bourdon and V. B. Cajipe. J. Solid State Chem. **141**, 290–293 (1998).

[S7] A. Grzechnik, V. B. Cajipe, C. Payen, and P. F. McMillan. Solid State Commun. **108**, 43–47 (1998).

[S8] M. Si, P. Y. Liao, G. Qiu, Y. Duan, and P. D. Ye. ACS Nano **12**, 6700–6705 (2018).

[S9] Y. M. Vysochanskii, V. Stephanovich, A. Molnar, V. Cajipe, and X. Bourdon. Phys. Rev. B **58**, 9119 (1998).

[S10] F. Liu, L. You, K. L. Seyler, X. Li, P. Yu, J. Lin, X. Wang, J. Zhou, H. Wang, H. He, S. T. Pantelides, W. Zhou, P. Sharma, X. Xu, P. M. Ajayan, J. Wang, and Z. Liu. Nat. Commun.

7, 1–6 (2016).

[S11] M. A. Susner, A. Belianinov, A. Borisevich, Q. He, M. Chyasnavichyus, H.Demir, D. S. Sholl, P. Ganesh, D. L. Abernathy, M. A. McGuire, *et al.* ACS Nano **9**, 12365–12373 (2015).

[S12] J. A. Brehm, S. M. Neumayer, L. Tao, A. O. Hara, M. Chyasnavichus, M. A. Susner, M. A. McGuire, S. V. Kalinin, S. Jesse, P. Ganesh, S. T. Pantelides, P. Maksymovych, and N. Balke. Nature Mater. **19**, 43–48 (2020).

[S13] S. M. Neumayer, J. A. Brehm, L. Tao, A. O'Hara, P. Ganesh, S. Jesse, M. A. Susner, M. A. McGuire, S. T. Pantelides, P. Maksymovych, and N. Balke. ACS Appl. Mater. Interfaces **12**, 38546–38553 (2020).

[S14] X. S. Xu, J. F. Ihlefeld, J. H. Lee, O. K. Ezekoye, E. Vlahos, R. Ramesh, V. Gopalan, X. Q. Pan, D. G. Schlom, and J. L. Musfeldt. Appl. Phys. **96**, 192901 (2010).

[S15] S. Neal, H-S. Kim, K. O'Neal, A. Haglund, K. Smith, D. Mandrus, H. Bechtel, G. L. Carr, K. Haule, D. Vanderbilt, and J. L. Musfeldt. Phys. Rev. B **102**, 085408 (2020).